JOURNAL OF AIRCRAFT
Vol. 31, No. 4, July–Aug. 1994

Airfoil Shaping for Reduced Radar Cross Section

Hoang Vinh,* C. P. van Dam,† and Harry A. Dwyer‡
University of California, Davis, Davis, California 95616

Field methods based on finite difference approximations of the time-domain Maxwell's equations and the potential-flow equation have been developed to evaluate the electromagnetic scattering and aerodynamic characteristics of airfoils. Strong similarities in the two analysis methods facilitate a synergistic approach to solve the multidisciplinary problem of airfoil shaping for aerodynamic efficiency and low radar cross section (RCS). Results for standard test cases demonstrate that both methods are quite accurate. A parametric study shows that for frontal radar illumination, the RCS of an airfoil is independent of the chordwise location of maximum thickness, but depends strongly on the maximum thickness, leading-edge radius, and leading-edge shape. In addition, the study shows that the RCS of an airfoil can be reduced without significant effects on its transonic aerodynamic efficiency by reducing the leading-edge radius and/or modifying the shape of the leading edge.

Nomenclature

a = radius of circular cylinder
C_D = sectional wave drag coefficient
CFL = Courant-Friedrichs-Lewy number, $c_0\Delta t/\Delta x$ in one dimension
C_L = sectional lift coefficient
C_p = static pressure coefficient
c = airfoil chord length
c_0 = electromagnetic wave speed in free space, $1/\sqrt{\mu_0\varepsilon_0}$
E_0 = incident electromagnetic wave amplitude
$\boldsymbol{E}$ = scattered electric-field intensity vector in time domain
$\boldsymbol{e}$ = scattered electric-field intensity vector in frequency domain
$\boldsymbol{H}$ = scattered magnetic-field intensity vector in time domain
J = coordinate transformation Jacobian, $\xi_x\eta_y - \xi_y\eta_x$
k = incident electromagnetic wave number, $2\pi/\lambda$
M_∞ = freestream Mach number
$\hat{\boldsymbol{n}}$ = unit vector along normal direction
R = distance from scattering object to observation point
t = time
u, v = velocity components in x, y directions
x, y = Cartesian coordinates
α = aerodynamic angle of attack
β = electromagnetic wave angle of incidence
γ = specific heat ratio
ε_0 = permittivity coefficient in free space
λ = incident electromagnetic wavelength
μ_0 = permeability coefficient in free space
ξ, η = azimuthal and radial coordinates of the generalized coordinate systems
ρ = fluid density
σ = radar cross section
ϕ = velocity potential function

Subscripts
i = spatial index
n = partial differentiation with respect to normal coordinate
t = partial differentiation with respect to t
x, y = partial differentiation with respect to x, y
ξ, η = partial differentiation with respect to ξ, η

Superscripts
i = incident-field value
n = time index
t = total-field value
x, y, z = components in x, y, z directions
$\perp$ = normal component
$\parallel$ = tangential component

Introduction

SINCE the early days of aviation, shaping for good aerodynamic characteristics has been an integral part of aircraft design. However, with the introduction of aircraft such as the Lockheed F-117A and the Northrop B-2, it is clear that low radar signature is also rapidly becoming an important criterion in the design of new aircraft. Thus, today the designer is not only faced with shaping for maximum aerodynamic efficiency, but also with shaping for low radar cross section (RCS). This multidisciplinary design problem requires accurate analyses of the aerodynamic and RCS characteristics of the entire aircraft. Reference 1 presents an excellent overview of the electromagnetic scattering mechanisms typical for an aircraft configuration as well as the various mathematical models which are available for evaluating the RCS. Hitzel[1] applied a relatively simple method based on the combined theory of geometrical and physical optics together with the superposition of solutions for basic shapes to determine the RCS of complex aircraft configurations. Unfortunately, this type of method is rather inaccurate, allowing only a first-order approximation of the radar signature. In this article, a field method based on finite difference approximations of the time-domain Maxwell's equations is used to determine the scattering characteristics of arbitrary two-dimensional configurations. This type of method is much more accurate and has the additional advantage that it is closely related to the aerodynamic prediction methods based on finite difference approximations of the Navier-Stokes equations or a reduced set of these equations. This similarity in the solution methods

Received April 24, 1993; revision received July 16, 1993; accepted for publication July 16, 1993.

*Graduate Research Assistant, Department of Mechanical and Aeronautical Engineering. Student Member AIAA.
†Associate Professor, Department of Mechanical and Aeronautical Engineering. Senior Member AIAA.
‡Professor, Department of Mechanical and Aeronautical Engineering. Senior Member AIAA.

allows a synergistic approach to solve the multidisciplinary problem of shaping for aerodynamic efficiency and low RCS.[2]

In the following section, the aerodynamic analysis method is briefly described. Next, a much more detailed description of the RCS analysis method is provided. Standard test cases have been solved to validate both methods and the results are presented to illustrate the capabilities and the obtainable accuracies of these methods. Finally, the two analysis methods are applied to study the effects of systematic changes in the geometry of airfoils on the transonic wave drag and the radar signature. The results of this study will provide the designer guidance in designing aerodynamically efficient airfoils with certain desired RCS characteristics. In addition, they will facilitate the development of an efficient multidisciplinary design method based on the present analysis methods and a numerical optimization technique.

Aerodynamic Analysis

The aerodynamic analysis is based on the finite difference solution of the conservative full-potential equation. The full-potential formulation is chosen over the more general Euler formulation because the full-potential equation is much less expensive to solve in terms of CPU time,[3] and yet gives very accurate prediction of wave drag at low transonic Mach numbers.[4] Numerous numerical methods have been developed for solving the transonic full-potential equation. Since these methods are described extensively in the literature (see Refs. 5 and 6 for a representative list of references), only a general description of one of the methods is presented here.

In two dimensions, the steady full-potential equation in Cartesian coordinates can be written in conservation form

$$(\rho\phi_x)_x + (\rho\phi_y)_y = 0 \tag{1}$$

where

$$\rho = \{1 - [(\gamma - 1)/2]M_\infty^2(u^2 + v^2 - 1)\}^{[1/(\gamma-1)]}$$
$$u = \phi_x \quad \text{and} \quad v = \phi_y \tag{2}$$

In this formulation, the density and velocity components are nondimensionalized by the freestream values. Equation (1) is solved subject to the surface tangency condition $\phi_n = 0$ at the body. In the present algorithm, Eqs. (1) and (2) are transformed to the generalized curvilinear coordinate system and discretized using second-order accurate central differences. The resulting system of nonlinear equations is linearized using Newton's method and solved iteratively for ϕ and ρ using the conventional successive-line-over-relaxation (SLOR) method.[6] At the end of each iteration, the circulation is computed from the potential jump at the trailing edge and imposed along the trailing-edge cut and the far-field boundary during the next iteration. To maintain numerical stability in the supersonic regions, artificial viscosity is added by upwind biasing the density as suggested by Holst.[7] The pressure distribution across the aerodynamic configuration is computed using the isentropic-flow equations. The lift and wave drag are calculated by integrating the surface pressure.

RCS Analysis

Governing Equations

The RCS analysis is based on the numerical solution of the time-domain Maxwell's curl equations. In this article, the analyses are restricted to scattering in free space. The corresponding Maxwell's equations for this case are

Ampere's law

$$(\varepsilon_0 \boldsymbol{E})_t - \nabla \times \boldsymbol{H} = 0 \tag{3}$$

Faraday's law

$$(\mu_0 \boldsymbol{H})_t + \nabla \times \boldsymbol{E} = 0 \tag{4}$$

These two coupled equations are transformed to the generalized curvilinear coordinate system and solved on body-conforming grids.

In three dimensions, the Maxwell's equations involve three components of the electric field (E^x, E^y, and E^z), and three components of the magnetic field (H^x, H^y, and H^z). In two dimensions, the Maxwell's equations decouple into the transverse-magnetic (TM) and transverse-electric (TE) modes. Electromagnetic waves corresponding to the TM mode are E-polarized and contain only the E^z, H^x, and H^y components, while TE waves are H-polarized and contain only the H^z, E^x, and E^y components. The two-dimensional Maxwell's equations in Cartesian coordinates can be written in conservation form following Shankar[8]:

$$\bar{\boldsymbol{Q}}_t + \bar{\boldsymbol{F}}_x + \bar{\boldsymbol{G}}_y = 0 \tag{5}$$

TM mode

$$\bar{\boldsymbol{Q}} = \begin{bmatrix} \varepsilon_0 E^z \\ \mu_0 H^x \\ \mu_0 H^y \end{bmatrix} \quad \bar{\boldsymbol{F}} = \begin{bmatrix} -H^y \\ 0 \\ -E^z \end{bmatrix} \quad \bar{\boldsymbol{G}} = \begin{bmatrix} H^x \\ E^z \\ 0 \end{bmatrix}$$

TE mode

$$\bar{\boldsymbol{Q}} = \begin{bmatrix} \mu_0 H^z \\ \varepsilon_0 E^x \\ \varepsilon_0 E^y \end{bmatrix} \quad \bar{\boldsymbol{F}} = \begin{bmatrix} E^y \\ 0 \\ H^z \end{bmatrix} \quad \bar{\boldsymbol{G}} = \begin{bmatrix} -E^x \\ -H^z \\ 0 \end{bmatrix}$$

As a result of the transformation from the Cartesian coordinate system to the generalized curvilinear coordinate system where $\xi = \xi(x, y)$ and $\eta = \eta(x, y)$, Eq. (5) becomes

$$\boldsymbol{Q}_t + \boldsymbol{F}_\xi + \boldsymbol{G}_\eta = 0 \tag{6}$$

TM mode

$$\boldsymbol{Q} = \frac{1}{J}\begin{bmatrix} \varepsilon_0 E^z \\ \mu_0 H^x \\ \mu_0 H^y \end{bmatrix} \quad \boldsymbol{F} = \frac{1}{J}\begin{bmatrix} \xi_y H^x - \xi_x H^y \\ \xi_y E^z \\ -\xi_x E^z \end{bmatrix}$$

$$\boldsymbol{G} = \frac{1}{J}\begin{bmatrix} \eta_y H^x - \eta_x H^y \\ \eta_y E^z \\ -\eta_x E^z \end{bmatrix}$$

TE mode

$$\boldsymbol{Q} = \frac{1}{J}\begin{bmatrix} \mu_0 H^z \\ \varepsilon_0 E^x \\ \varepsilon_0 E^y \end{bmatrix} \quad \boldsymbol{F} = \frac{1}{J}\begin{bmatrix} \xi_x E^y - \xi_y E^x \\ -\xi_y H^z \\ \xi_x H^z \end{bmatrix}$$

$$\boldsymbol{G} = \frac{1}{J}\begin{bmatrix} \eta_x E^y - \eta_y E^x \\ -\eta_y H^z \\ \eta_x H^z \end{bmatrix}$$

where the vectors $\boldsymbol{F}$ and $\boldsymbol{G}$ can be written as functions of Q

$$\boldsymbol{F} = \boldsymbol{A}\boldsymbol{Q} \tag{7}$$

$$\boldsymbol{G} = \boldsymbol{B}\boldsymbol{Q} \tag{8}$$

TM mode

$$A = \begin{bmatrix} 0 & \frac{\xi_y}{\mu_0} & -\frac{\xi_x}{\mu_0} \\ \frac{\xi_y}{\varepsilon_0} & 0 & 0 \\ -\frac{\xi_x}{\varepsilon_0} & 0 & 0 \end{bmatrix} \quad B = \begin{bmatrix} 0 & \frac{\eta_y}{\mu_0} & -\frac{\eta_x}{\mu_0} \\ \frac{\eta_y}{\varepsilon_0} & 0 & 0 \\ -\frac{\eta_x}{\varepsilon_0} & 0 & 0 \end{bmatrix}$$

TE mode

$$A = \begin{bmatrix} 0 & -\frac{\xi_y}{\varepsilon_0} & \frac{\xi_x}{\varepsilon_0} \\ -\frac{\xi_y}{\mu_0} & 0 & 0 \\ \frac{\xi_x}{\mu_0} & 0 & 0 \end{bmatrix} \quad B = \begin{bmatrix} 0 & -\frac{\eta_y}{\varepsilon_0} & \frac{\eta_x}{\varepsilon_0} \\ -\frac{\eta_y}{\mu_0} & 0 & 0 \\ \frac{\eta_x}{\mu_0} & 0 & 0 \end{bmatrix}$$

Equation (6) can be solved numerically using any one of the numerous CFD-based finite difference methods which have been developed for hyperbolic equations.[6] Here, the Lax-Wendroff scheme is used. This explicit scheme is computationally efficient and is generally less dispersive than implicit schemes.[9] In addition, it is easily extendible to multidimensions.

Lax-Wendroff Scheme

The Lax-Wendroff scheme is an explicit scheme widely used in CFD. It is second-order accurate in both time and space. For the one-dimensional Maxwell's equations

$$\bar{Q}_t + \bar{F}_x = 0 \tag{9}$$

where

$$\bar{Q} = \begin{bmatrix} \varepsilon_0 E^z \\ \mu_0 H^y \end{bmatrix} \quad \bar{F} = \bar{A}\bar{Q} = \begin{bmatrix} -H^y \\ -E^z \end{bmatrix} \quad \bar{A} = \begin{bmatrix} 0 & -\frac{1}{\mu_0} \\ -\frac{1}{\varepsilon_0} & 0 \end{bmatrix}$$

the Lax-Wendroff algorithm is derived starting from the Taylor-series expansion

$$\bar{Q}_i^{n+1} = \bar{Q}_i^n + \Delta t \bar{Q}_t + (\Delta t^2/2)\bar{Q}_{tt} + \mathcal{O}(\Delta t^3) \tag{10}$$

Using Eq. (9), the time derivatives in Eq. (10) are replaced with spatial derivatives

$$\bar{Q}_t = -\bar{F}_x \tag{11}$$

$$\bar{Q}_{tt} = -\bar{F}_{tx} = -\bar{A}\bar{Q}_{tx} = \bar{A}\bar{F}_{xx} \tag{12}$$

Thus Eq. (10) becomes

$$\bar{Q}_i^{n+1} = \bar{Q}_i^n - \Delta t \bar{F}_x + (\Delta t^2/2)\bar{A}\bar{F}_{xx} \tag{13}$$

Finally, the Lax-Wendroff algorithm for the one-dimensional Maxwell's equations is obtained by replacing the spatial derivatives in Eq. (13) with central-difference approximations

$$\bar{Q}_i^{n+1} = \bar{Q}_i^n - \Delta t \frac{\bar{F}_{i+1}^n - \bar{F}_{i-1}^n}{2\Delta x} + \frac{\Delta t^2}{2}\bar{A}\frac{\bar{F}_{i+1}^n - 2\bar{F}_i^n + \bar{F}_{i-1}^n}{\Delta x^2} \tag{14}$$

Note that in this case the Jacobian matrix $\bar{A}$ is constant. In Eqs. (7) and (8), the Jacobian matrices A and B are functions of the spatial variables ξ and η.

In one dimension, the Lax-Wendroff scheme is numerically stable for CFL ≤ 1. Therefore, the maximum allowable time step for the Lax-Wendroff scheme, and all explicit schemes in general, is directly dependent on the resolution of the computational grid. In addition, the Lax-Wendroff scheme is both dissipative and dispersive, but these numerical errors are small near the stability limit. In general, the derivation of the Lax-Wendroff algorithm for the one-dimensional Maxwell's equations presented here can be extended directly to multidimensions.

Boundary Conditions

For perfectly-conducting scatterers, the reflecting boundary conditions for the electric and magnetic fields at the body are, respectively

$$\hat{n} \times E^t = 0 \tag{15}$$

$$\hat{n} \cdot H^t = 0 \tag{16}$$

Here, the total field represents the sum of the incident and scattered fields. Equations (15) and (16) imply that the tangential component of the total electric field and the normal component of the total magnetic field both vanish at the body

$$E^{\parallel,t} = E^{\parallel} + E^{\parallel,i} = 0 \tag{17}$$

$$H^{\perp,t} = H^{\perp} + H^{\perp,i} = 0 \tag{18}$$

In general, it is more advantageous to solve the Maxwell's equations in terms of the scattered field. Due to the dispersive nature of most finite difference schemes, dispersion error grows as the electromagnetic wave is propagated numerically through a curvilinear mesh. To minimize dispersion error, a scattered-field formulation is used in which the incident field is propagated analytically and only the scattered field is computed. Using the scattered-field formulation, the boundary conditions given by Eqs. (17) and (18) become

$$E^{\parallel} = -E^{\parallel,i} \tag{19}$$

$$H^{\perp} = -H^{\perp,i} \tag{20}$$

In this article, the incident electromagnetic wave is represented by a sinusoidal plane wave[8]:

TM mode

$$E^{z,i} = E_0 \sin[k(x \cos\beta + y \sin\beta - c_0 t)]$$
$$H^{x,i} = \frac{E^{z,i}\sin\beta}{\mu_0 c_0}, \qquad H^{y,i} = -\frac{E^{z,i}\cos\beta}{\mu_0 c_0} \tag{21}$$

TE mode

$$H^{z,i} = E_0 \sin[k(x \cos\beta + y \sin\beta - c_0 t)]$$
$$E^{x,i} = -\frac{H^{z,i}\sin\beta}{\varepsilon_0 c_0}, \qquad E^{y,i} = \frac{H^{z,i}\cos\beta}{\varepsilon_0 c_0} \tag{22}$$

where the quantities E_0, μ_0, ε_0, and c_0 are all normalized to unity.

At the outer boundary, the approximate absorbing boundary condition derived by Mur[10] is imposed to allow scattered waves to propagate out of the computational domain

$$\psi_t + c_0 \psi_\eta = 0 \tag{23}$$

where

$$\psi(\text{TM mode}) = \begin{bmatrix} E^z \\ H^x \\ H^y \end{bmatrix} \quad \psi(\text{TE mode}) = \begin{bmatrix} H^z \\ E^x \\ E^y \end{bmatrix}$$

Since this is only an approximation of a perfectly absorbing boundary, the outer boundary must be placed sufficiently far away from the scatterer to minimize the effects of any wave reflection.

RCS Evaluation

Electromagnetic radiation is scattered from an object with varying intensities in different directions. The RCS is a measurement of the intensity of the scattered wave with respect to the impinging signal. When the directions of illumination and observation are identical, the RCS is called backscatter or monostatic RCS. When the radar transmitter and receiver are not collocated, the RCS is called bistatic RCS. In two dimensions, RCS is defined as[11]

$$\sigma = \lim_{R\to\infty} 2\pi R \frac{|e(R)|^2}{|e^i|^2} \tag{24}$$

Normally, RCS is expressed in decibels: σ (dB) = $10 \log_{10}\sigma$. Note that the scattered electric-field intensity is a function of R, and RCS is defined for R approaching infinity. Since the Maxwell's equations are solved for a finite domain, only the scattered electric field near the scattering object is known. This so-called near-field solution is transformed to the far field using the Green's function transform. In addition, note that RCS is defined in the frequency domain. Thus, the time-dependent solution of the Maxwell's equations must be transformed into frequency domain in order to calculate the RCS. In the present analyses, the numerical solution of the Maxwell's equations is saved for one complete wave cycle after periodic steady state has been reached. The time-domain solution is then transformed into frequency domain using the discrete Fourier transform. To minimize the effect of numerical errors, the RCS is evaluated using field values taken at the surface of the scatterer.

Code Validation

The aerodynamic and RCS analysis algorithms have been validated using standard test cases. The test case for the aerodynamic analysis involves transonic flow over the lifting NACA-0012 airfoil at $M_\infty = 0.75$ and $\alpha = 2.0$ deg. The computational grid is relatively coarse containing 140 × 30 points. The outer boundary is located at 10 chord lengths from the airfoil. The airfoil has been extended to a sharp trailing edge and renormalized to unit chord length. The computed surface pressure coefficient distribution along with the lift and drag coefficients of the airfoil are shown in Fig. 1. Both the lift and drag coefficients are in good agreement with the results presented by Holst in Ref. 7.

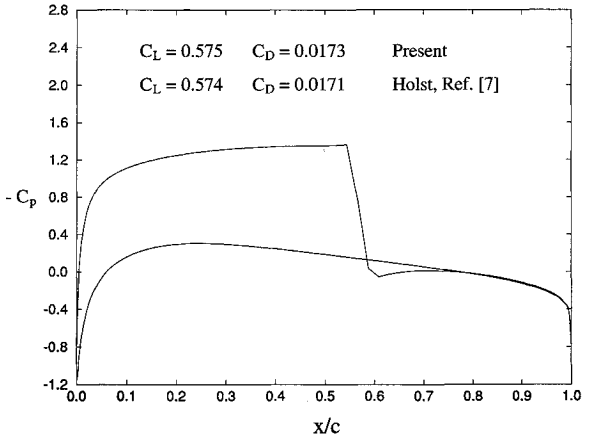

Fig. 1 Surface pressure coefficient distribution on the NACA-0012 airfoil ($M_\infty = 0.75$, $\alpha = 2.0$ deg).

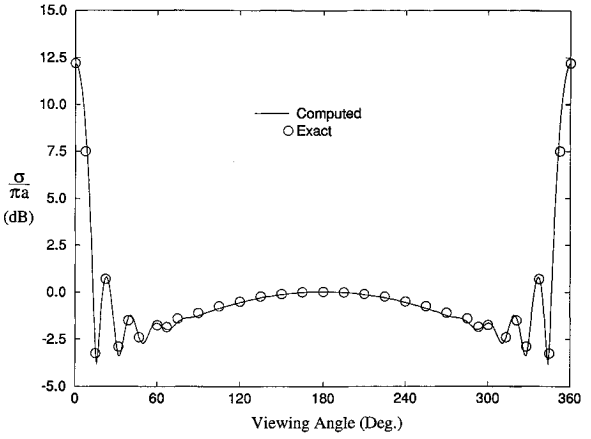

Fig. 2 Bistatic RCS of a perfectly-conducting, infinite circular cylinder (TM mode, $ka = 10$).

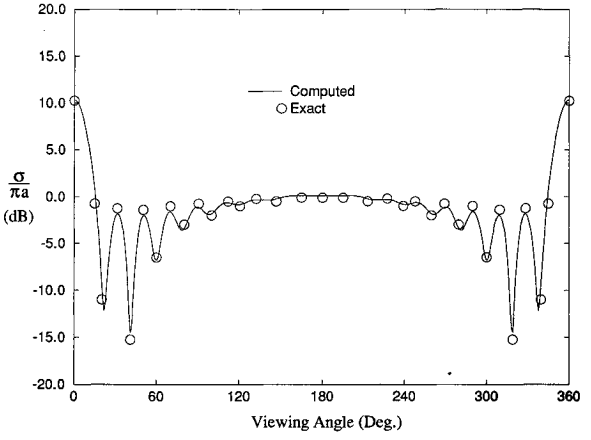

Fig. 3 Bistatic RCS of a perfectly-conducting, infinite circular cylinder (TE mode, $ka = 10$).

The test case for the RCS analysis involves a right-propagating plane wave impinging a perfectly conducting, infinite circular cylinder. The cylinder has an electrical size of $ka = 10$. The computational grid contains 150 × 75 points with the outer boundary located at 5λ from the cylinder surface. The computed bistatic RCS of the cylinder corresponding to the TM and TE modes are shown in Figs. 2 and 3, respectively, along with the exact solutions.[12] Overall, the computed results are in excellent agreement with the exact solutions.

Parametric Study

The aerodynamic and RCS analysis algorithms are applied to study the effects of maximum thickness, leading-edge radius, and leading-edge shape of an airfoil on its aerodynamic efficiency and radar signature. In each case, the airfoil is extended to a sharp trailing edge and renormalized to unit chord length. The computational grid used for the aerodynamic analysis contains 140 × 30 points with the outer boundary located at 10 chord lengths from the airfoil. In the RCS analysis, the airfoil is illuminated from the front by a right-propagating plane wave with a wavelength of $\lambda = 0.25c$. The computational grid used for this part of analysis contains 120 × 60 points with the outer boundary located at approximately 4λ from the airfoil. In order to limit the length of the paper, only results for the TM mode are presented in this study.

Effects of Maximum Thickness Location

The effects of maximum thickness location on the aerodynamic and RCS characteristics of airfoils are examined using the NACA-0012 and NACA-0012-64 airfoils[13] shown in Fig. 4. Both airfoils have a maximum thickness of $0.12c$ and

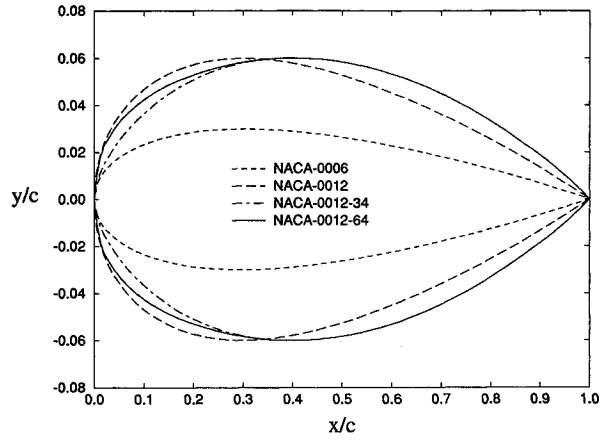

Fig. 4 NACA 4-digit series airfoils used in the parametric study.

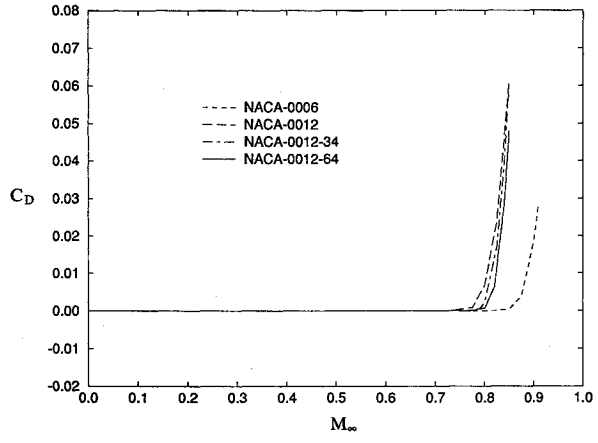

Fig. 5 Variations of wave drag coefficient with freestream Mach number for the NACA 4-digit series airfoils (α = 0.0 deg).

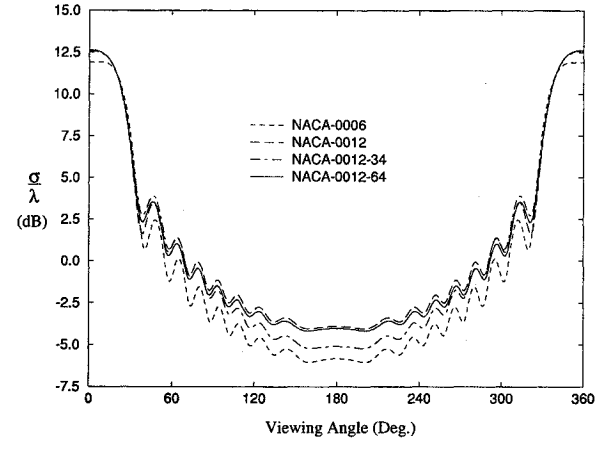

Fig. 6 Bistatic RCS of the NACA 4-digit series airfoils (TM mode, $\lambda = 0.25c$).

a leading-edge radius of 0.0158c. However, the maximum thickness of the NACA-0012 airfoil is located at 30% of the chord, whereas the maximum thickness of the NACA-0012-64 airfoil is located at 40% of the chord. Thus, the two airfoils differ only in their maximum thickness location.

The computed wave drag coefficients of the two airfoils at zero angle of attack are shown in Fig. 5 as a function of the freestream Mach number. The wave drag of each airfoil is zero or near zero up to the drag-divergence Mach number where it increases rapidly due to shock wave action in the flowfield. Figure 5 shows that the drag-divergence Mach number increases slightly as the maximum thickness location of the airfoil is moved aft toward the trailing edge. The computed bistatic RCS of the two airfoils are shown in Fig. 6 where the 180-deg viewing angle corresponds to the leading edge, and the 0/360-deg viewing angle coincides with the trailing edge. Figure 6 shows that the chordwise location of maximum thickness has no significant effect on the airfoil radar signature, especially in the backscatter region around the 180-deg viewing angle which is often the most important threat sector for aircraft.

Effects of Maximum Thickness

This study involves the NACA-0006 and NACA-0012-34 airfoils[13] shown in Fig. 4. These two airfoils have nearly identical leading-edge radii: 0.00397c (NACA-0006) and 0.00391c (NACA-0012-34). The maximum thickness of the NACA-0006 airfoil is 0.06c at 30% of the chord, whereas the NACA-0012-34 airfoil has a maximum thickness of 0.12c at 40% of the chord. Since it was found in the previous section that the chordwise location of maximum thickness has only a minor effect on the drag-divergence Mach number and virtually no effect on the bistatic RCS, these two airfoils are good candidates for studying the effects of maximum thickness on the aerodynamic and RCS characteristics of airfoils.

The computed wave drag coefficients of the two airfoils at zero angle of attack are shown in Fig. 5 as a function of the freestream Mach number. As expected, the drag-divergence Mach number increases significantly as the maximum thickness is decreased. The computed RCS responses of the two airfoils, shown in Fig. 6, reveal that the bistatic RCS decreases as the maximum thickness of the airfoil is decreased. Therefore, the thinner airfoil not only has a higher drag-divergence Mach number, but also a smaller radar signature than the thicker airfoil.

Effects of Leading-Edge Radius

The NACA-0012 and NACA-0012-34 airfoils with leading-edge radii of 0.0158c and 0.00391c, respectively, are used in this study to examine the effects of leading-edge radius on the airfoil aerodynamic efficiency and radar signature. The two airfoils are shown in Fig. 4. Both airfoils have a maximum thickness of 0.12c, although at different chord positions. Again, the chordwise location of maximum thickness of the two airfoils is considered to have negligible effects on their aerodynamic and RCS characteristics.

The computed wave drag coefficients of the two airfoils at zero angle of attack are shown in Fig. 5 as a function of the freestream Mach number. The NACA-0012-34 airfoil has a slightly higher drag-divergence Mach number than the NACA-0012 airfoil. It should be noted that an increase in leading-edge radius is not necessarily accompanied by an increase in drag nor a decrease in drag-divergence Mach number.[14] The biggest difference between these two airfoils is in their bistatic RCS shown in Fig. 6. The bistatic RCS in the backscatter region of the NACA-0012-34 airfoil is lower than that of the NACA-0012 airfoil, demonstrating that not only the maximum thickness but also the leading-edge radius is a critical parameter in the design of low-observable airfoils.

Effects of Leading-Edge Shape

The results presented in the previous sections illustrate that the aerodynamic and RCS analysis algorithms are very useful tools for analyzing the effects of shaping on the aerodynamic and RCS characteristics of airfoils. Here, an example is presented to show how these analysis methods can be used to design aerodynamically efficient airfoils with reduced RCS. The example is based on a 12% thick supercritical airfoil.[15] The main objective here is to reduce the airfoil radar signature (based on frontal illumination) while maintaining its aerodynamic efficiency by modifying the shape of the leading edge. The baseline airfoil is shown in Fig. 7 along with the modified airfoil. The modification made to the baseline airfoil is the

Table 1 Lift and drag coefficients

Airfoil	C_L	C_D
Baseline	0.6262	0.00161
Modified	0.6266	0.00161

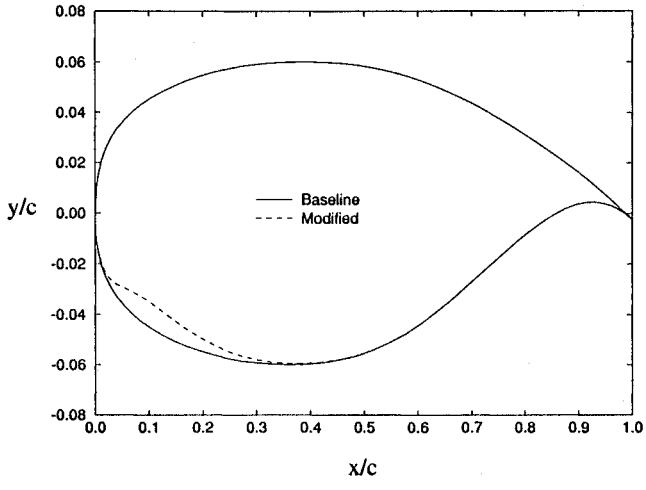

Fig. 7 Baseline and modified airfoil shapes.

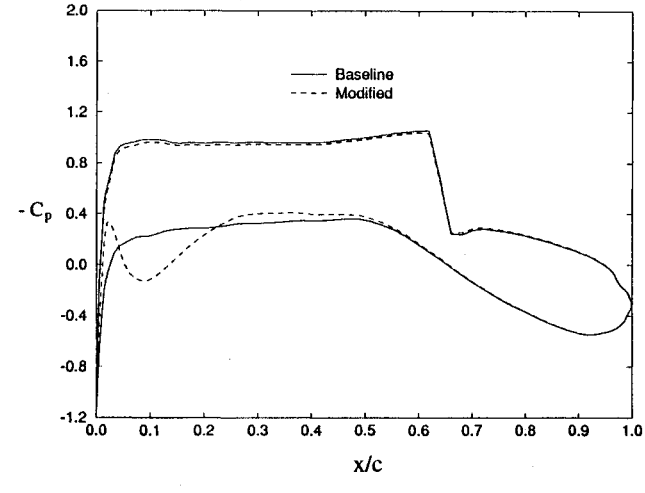

Fig. 8 Surface pressure coefficient distributions on the baseline and modified airfoils [$M_\infty = 0.76$, $\alpha = 0.0$ deg (baseline), $\alpha = -0.03$ deg (modified)].

undercut in the front section of the lower surface. Note that the two airfoils have identical leading-edge radius and maximum thickness. The aerodynamic analysis of the baseline airfoil is done for the freestream condition of $M_\infty = 0.76$ and $\alpha = 0.0$ deg. The aerodynamic characteristics of the modified airfoil are evaluated for the same freestream Mach number, but at a slightly negative angle of attack ($\alpha = -0.03$ deg) in order to maintain the same lift coefficient as in the case of the baseline airfoil. The computed surface pressure coefficient distributions of the two airfoils are compared in Fig. 8. The corresponding lift and drag coefficients of the baseline and modified 12% thick supercritical airfoils at $M_\infty = 0.76$ are listed in Table 1. The modified leading edge has no significant effect on the wave drag. The bistatic RCS of the two airfoils are shown in Fig. 9. They indicate that the undercut in the lower leading edge of the modified airfoil reduces its RCS over a wide range of viewing angles. This example illustrates that the radar signature of an airfoil can be reduced without significant effects on its transonic aerodynamic efficiency by appropriately modifying the shape of the leading edge.

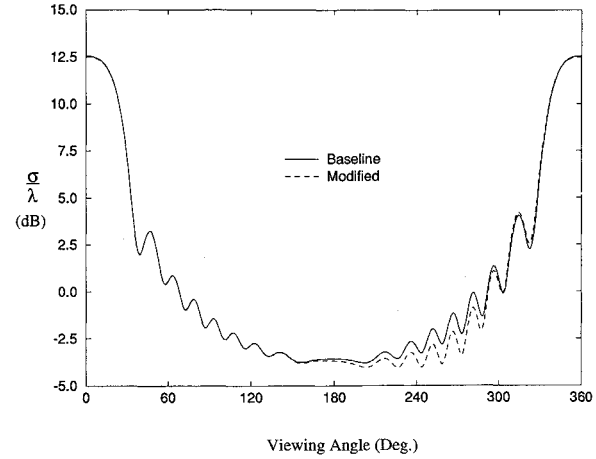

Fig. 9 Bistatic RCS of the baseline and modified airfoils (TM mode, $\lambda = 0.25c$).

Conclusions

Finite difference methods for analyzing the aerodynamic efficiency and RCS characteristics of arbitrary two-dimensional configurations have been developed. These methods allow a synergistic approach to solve the multidisciplinary problem of airfoil shaping for aerodynamic efficiency and low RCS. The two analysis methods have been applied to study the effects of systematic changes in the geometry of airfoils on the transonic wave drag and the radar signature. The results of this parametric study show that for frontal radar illumination, the RCS of an airfoil is independent of the chordwise location of maximum thickness but depends strongly on the maximum thickness, leading-edge radius, and leading-edge shape. The study also shows that the RCS of an airfoil can be reduced without significant effects on its transonic aerodynamic efficiency by appropriately reducing the leading-edge radius and/or modifying the shape of the leading edge. These results will provide the designer guidance in designing aerodynamically efficient airfoils with certain desired RCS characteristics. In addition, they will facilitate the development of an efficient multidisciplinary design method based on the present analysis methods and a numerical optimization technique.

Acknowledgment

This research has been supported by the NASA Ames Research Center under Joint Research Interchange Agreements NCA2-568 and NCA2-581.

References

[1]Hitzel, S. M., "Aerodynamics and Radar Signature: A Combination of Theoretical Methods," *Journal of Aircraft*, Vol. 25, No. 5, 1988, pp. 399–404.

[2]Shankar, V., Hall, W., and Mohammadian, A. H., "A CFD-Based Finite-Volume Procedure for Computational Electromagnetics—Interdisciplinary Applications of CFD Methods," *Proceedings of the AIAA 9th Computational Fluid Dynamics Conference*, AIAA, Washington, DC, 1989, pp. 551–564 (AIAA Paper 89-1987).

[3]Flores, J., Barton, J., Holst, T., and Pulliam, T., "Comparison of the Full-Potential and Euler Formulations for Computing Transonic Airfoil Flows," NASA TM 85983, June 1984.

[4]Slooff, J. W., "Computational Drag Analysis and Minimization; Mission Impossible?," *Aircraft Drag Prediction and Reduction*, AGARD R-723, Addendum I, 1986.

[5]Hirsch, C., *Numerical Computation of Internal and External Flows*, Vol. 2, Wiley, Chichester, England, UK, 1990, pp. 57–121.

[6]Anderson, D. A., Tannehill, J. C., and Pletcher, R. H., *Computational Fluid Mechanics and Heat Transfer*, Hemisphere, New York, 1984, pp. 87–107, 134–135, 302–318.

[7]Holst, T. L., "Implicit Algorithm for the Conservative Transonic

Full-Potential Equation Using an Arbitrary Mesh," *AIAA Journal*, Vol. 17, No. 10, 1979, pp. 1038–1045.

[8]Shankar, V., Hall, W. F., and Mohammadian, A. H., "A Time-Domain Differential Solver for Electromagnetic Scattering Problems," *Radar Cross Sections of Complex Objects*, edited by W. R. Stone, IEEE Press, New York, 1990, pp. 127–139.

[9]Vinh, H., Dwyer, H. A., and Van Dam, C. P., "Finite-Difference Algorithms for the Time-Domain Maxwell's Equations—A Numerical Approach to RCS Analysis," AIAA Paper 92-2989, July 1992.

[10]Mur, G., "Absorbing Boundary Conditions for the Finite-Difference Approximation of the Time-Domain Electromagnetic-Field Equations," *IEEE Transactions on Electromagnetic Compatibility*, Vol. EMC-23, No. 4, 1981, pp. 377–382.

[11]Knott, E. F., "Radar Cross Section," *Aspects of Modern Radar*, edited by E. Brookner, Artech House, Boston, MA, 1988, p. 416.

[12]Ruck, G. T., Barrick, D. E., Stuart, W. D., and Krichbaum, C. K., *Radar Cross Section Handbook*, Vol. 1, Plenum Press, New York, 1970, p. 212.

[13]Abbott, I. H., and Von Doenhoff, A. E., *Theory of Wing Sections*, Dover, New York, 1959, pp. 311–323.

[14]Wilby, P. G., "The Pressure Drag of an Aerofoil with Six Different Round Leading Edges, at Transonic and Low Supersonic Speeds," British ARC CP 921, Jan. 1966.

[15]Harris, C. D., "NASA Supercritical Airfoils—A Matrix of Family-Related Airfoils," NASA TP 2969, March 1990.